

PAPER

F Y X i W] b [' g WU h h Y f Y X ' `] [\ h

f i b

To cite this article: S Soni *et al* 2021 *Class. Quantum Grav.* **38** 025016

View the [article online](#) for updates and enhancements.

You may also like

- [The ATLAS Fast Tracker system](#)
The ATLAS collaboration, G. Aad, B. Abbott et al.
- [Operation and performance of the ATLAS semiconductor tracker in LHC Run 2](#)
The ATLAS collaboration, Georges Aad, Brad Abbott et al.



IOP | ebooks™

Bringing together innovative digital publishing with leading authors from the global scientific community.

Start exploring the collection—download the first chapter of every title for free.

Reducing scattered light in LIGO's third observing run

S Soni^{1,*}, C Austin¹, A Effler², R M S Schofield³,
G González¹, V V Frolov², J C Driggers⁴, A Pele²,
A L Urban¹, G Valdes¹, R Abbott⁵, C Adams², R X Adhikari⁵,
A Ananyeva⁵, S Appert⁵, K Arai⁵, J S Areeda⁶, Y Asali⁷,
S M Aston², A M Baer⁸, M Ball³, S W Ballmer⁹, S Banagiri¹⁰,
D Barker⁴, L Barsotti¹¹, J Bartlett⁴, B K Berger¹²,
J Betzwieser², D Bhattacharjee¹³, G Billingsley⁵,
S Biscans^{11,5}, C D Blair², R M Blair⁴, N Bode^{14,15},
P Booker^{14,15}, R Bork⁵, A Bramley², A F Brooks⁵,
D D Brown¹⁶, A Buikema¹¹, C Cahillane⁵, K C Cannon¹⁷,
X Chen¹⁸, A A Ciobanu¹⁶, F Clara⁴, S J Cooper¹⁹,
K R Corley⁷, S T Countryman⁷, P B Covas²⁰, D C Coyne⁵,
L E H Datrier²¹, D Davis⁹, C Di Fronzo¹⁹, K L Dooley^{22,23},
P Dupej²¹, S E Dwyer⁴, T Etzel⁵, M Evans¹¹, T M Evans²,
J Feicht⁵, A Fernandez-Galiana¹¹, P Fritschel¹¹, P Fulda²⁴,
M Fyffe², J A Giaime^{1,2}, K D Giardina², P Godwin²⁵,
E Goetz^{1,13}, S Gras¹¹, C Gray⁴, R Gray²¹, A C Green²⁴,
E K Gustafson⁵, R Gustafson²⁶, J Hanks⁴, J Hanson²,
T Hardwick¹, R K Hasskew², M C Heintze²,
A F Helmling-Cornell³, N A Holland²⁷, J D Jones⁴,
S Kandhasamy²⁸, S Karki³, M Kasprzak⁵, K Kawabe⁴,
N Kijbunchoo²⁷, P J King⁴, J S Kissel⁴, Rahul Kumar⁴,
M Landry⁴, B B Lane¹¹, B Lantz¹², M Laxen²,
Y K Lecoecuche⁴, J Leviton²⁶, J Liu^{14,15}, M Lormand²,
A P Lundgren²⁹, R Macas²², M MacInnis¹¹, D M Macleod²²,
G L Mansell^{4,11}, S Márka⁷, Z Márka⁷, D V Martynov¹⁹,
K Mason¹¹, T J Massinger¹¹, F Matichard^{5,11}, N Mavalvala¹¹,
R McCarthy⁴, D E McClelland²⁷, S McCormick²,
L McCuller¹¹, J McIver⁵, T McRae²⁷, G Mendell⁴, K Merfeld³,
E L Merilh⁴, F Meylahn^{14,15}, T Mistry³⁰, R Mittleman¹¹,
G Moreno⁴, C M Mow-Lowry¹⁹, S Mozzon²⁹, A Mullavey²,
T J N Nelson², P Nguyen³, L K Nuttall²⁹, J Oberling⁴,
Richard J Oram², C Osthelder⁵, D J Ottaway¹⁶,
H Overmier², J R Palamos³, W Parker^{2,31}, E Payne³²,
R Penhorwood²⁶, C J Perez⁴, M Pirello⁴, H Radkins⁴,
K E Ramirez³³, J W Richardson⁵, K Riles²⁶,

*Author to whom any correspondence should be addressed.

**N A Robertson^{5,21}, J G Rollins⁵, C L Romel⁴, J H Romie²,
M P Ross³⁴, K Ryan⁴, T Sadecki⁴, E J Sanchez⁵,
L E Sanchez⁵, T R Saravanan²⁸, R L Savage⁴, D Schaetzl⁵,
R Schnabel³⁵, E Schwartz², D Sellers², T Shaffer⁴, D Sigg⁴,
B J J Slagmolen²⁷, J R Smith⁶, B Sorazu²¹, A P Spencer²¹,
K A Strain²¹, L Sun⁵, M J Szczepańczyk²⁴, M Thomas²,
P Thomas⁴, K A Thorne², K Toland²¹, C I Torrie⁵, G Traylor²,
M Tse¹¹, G Vajente⁵, D C Vander-Hyde⁹, P J Veitch¹⁶,
K Venkateswara³⁴, G Venugopalan⁵, A D Viets³⁶, T Vo⁹,
C Vorvick⁴, M Wade³⁷, R L Ward²⁷, J Warner⁴, B Weaver⁴,
R Weiss¹¹, C Whittle¹¹, B Willke^{15,14}, C C Wipf⁵, L Xiao⁵,
H Yamamoto⁵, Hang Yu¹¹, Haocun Yu¹¹, L Zhang⁵,
M E Zucker^{11,5}, J Zweizig⁵ and (The LIGO Scientific
Collaboration)**

¹ Louisiana State University, Baton Rouge, LA 70803, United States of America

² LIGO Livingston Observatory, Livingston, LA 70754, United States of America

³ University of Oregon, Eugene, OR 97403, United States of America

⁴ LIGO Hanford Observatory, Richland, WA 99352, United States of America

⁵ LIGO, California Institute of Technology, Pasadena, CA 91125, United States of America

⁶ California State University Fullerton, Fullerton, CA 92831, United States of America

⁷ Columbia University, New York, NY 10027, United States of America

⁸ Christopher Newport University, Newport News, VA 23606, United States of America

⁹ Syracuse University, Syracuse, NY 13244, United States of America

¹⁰ University of Minnesota, Minneapolis, MN 55455, United States of America

¹¹ LIGO, Massachusetts Institute of Technology, Cambridge, MA 02139, United States of America

¹² Stanford University, Stanford, CA 94305, United States of America

¹³ Missouri University of Science and Technology, Rolla, MO 65409, United States of America

¹⁴ Max Planck Institute for Gravitational Physics (Albert Einstein Institute), D-30167 Hannover, Germany

¹⁵ Leibniz Universität Hannover, D-30167 Hannover, Germany

¹⁶ OzGrav, University of Adelaide, Adelaide, South Australia 5005, Australia

¹⁷ RESCEU, University of Tokyo, Tokyo, 113-0033, Japan

¹⁸ OzGrav, University of Western Australia, Crawley, Western Australia 6009, Australia

¹⁹ University of Birmingham, Birmingham B15 2TT, United Kingdom

²⁰ Universitat de les Illes Balears, IAC3—IEEC, E-07122 Palma de Mallorca, Spain

²¹ SUPA, University of Glasgow, Glasgow G12 8QQ, United Kingdom

²² Cardiff University, Cardiff CF24 3AA, United Kingdom

²³ The University of Mississippi, University, MS 38677, United States of America

²⁴ University of Florida, Gainesville, FL 32611, United States of America

²⁵ The Pennsylvania State University, University Park, PA 16802, United States of America

²⁶ University of Michigan, Ann Arbor, MI 48109, United States of America

²⁷ OzGrav, Australian National University, Canberra, Australian Capital Territory 0200, Australia

- ²⁸ Inter-University Centre for Astronomy and Astrophysics, Pune 411007, India
²⁹ University of Portsmouth, Portsmouth, PO1 3FX, United Kingdom
³⁰ The University of Sheffield, Sheffield S10 2TN, United Kingdom
³¹ Southern University and A & M College, Baton Rouge, LA 70813, United States of America
³² OzGrav, School of Physics & Astronomy, Monash University, Clayton 3800, Victoria, Australia
³³ The University of Texas Rio Grande Valley, Brownsville, TX 78520, United States of America
³⁴ University of Washington, Seattle, WA 98195, United States of America
³⁵ Universität Hamburg, D-22761 Hamburg, Germany
³⁶ Concordia University Wisconsin, 2800 N Lake Shore Dr, Mequon, WI 53097, United States of America
³⁷ Kenyon College, Gambier, OH 43022, United States of America

E-mail: siddharthsoni22@gmail.com

Received 14 August 2020, revised 18 October 2020

Accepted for publication 10 November 2020

Published 14 December 2020



CrossMark

Abstract

Noise due to scattered light has been a frequent disturbance in the advanced LIGO gravitational wave detectors, hindering the detection of gravitational waves. The non stationary scatter noise caused by low frequency motion can be recognized as arches in the time-frequency plane of the gravitational wave channel. In this paper, we characterize the scattering noise for LIGO and Virgo's third observing run O3 from April, 2019 to March, 2020. We find at least two different populations of scattering noise and we investigate the multiple origins of one of them as well as its mitigation. We find that relative motion between two specific surfaces is strongly correlated with the presence of scattered light and we implement a technique to reduce this motion. We also present an algorithm using a witness channel to identify the times this noise can be present in the detector.

Keywords: scattered light, LIGO, ground motion, interferometry

(Some figures may appear in colour only in the online journal)

1. Introduction

The LIGO gravitational-wave observatories located at Hanford, Washington (LHO), and Livingston, Louisiana (LLO) in the USA [1], along with the Virgo detector in Cascina, Italy [2], and the GEO 600 detector in Germany [3] are a part of a worldwide network of gravitational-wave detectors. A schematic of the LIGO detectors is shown in figure 1. Each LIGO detector is a dual-recycled Fabry–Perot Michelson interferometer with 4 km arms. The detector acts as a transducer for strain, converting phase shift due to a gravitational wave into a signal that can be measured on a photo-diode. The output signal at the photodetectors is calibrated to an equivalent strain signal $h(t)$ [4, 5].

The first two observing runs, in September 2015–January 2016 and November 2016–August 2017, resulted in spectacular discoveries, including signals from the merger of

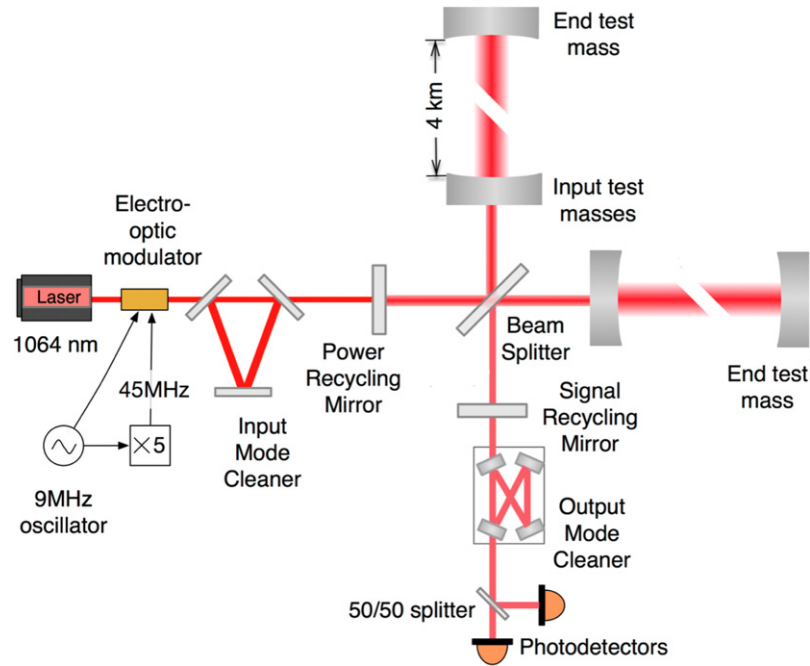


Figure 1. A schematic of aLIGO detectors taken from [6].

10 pairs of black holes and one from a merger of neutrons stars [7–9]. The third observing run began on April 1, 2019, and ended on March 27, 2020. During this run, plausible gravitational wave sources were shared as public alerts, averaging one a week [10]. The average binary neutron star (BNS) range at Livingston and Hanford, during O3, is approximately 130 Mpc and 110 Mpc respectively. In October 2019, a month-long working break separated the first and second half of O3, called O3a and O3b respectively. An increase in the laser input power and squeezed light injection contributed to the increase in range from O2 to O3 [11].

Noise from several different sources limits the sensitivity of the strain data at different frequencies. While quantum shot noise is dominant at frequencies above 300 Hz [12], ground motion is the major source of noise below 10 Hz which can affect the higher frequency band of the detectors. In addition to quantum noise, suspension noise and seismic noise, short duration noise transients also known as ‘glitches’ can affect the sensitivity of the detectors [13]. These noise transients can be due to high ground motion, electronic malfunction or other reasons, not well-understood [14–16]. At aLIGO they are detected by the Omicron algorithm. Each of these glitches, also known as omicron trigger, is annotated with some parameters such as event time, frequency, signal to noise ratio (SNR) [17–19]. In this paper, we focus on the type of noise transient due to scattered light which impacts the gravitational strain in 10 Hz to 120 Hz frequency band. Signals from the merger of very massive binary black holes may fall into this frequency region [20]. Thus, identifying and reducing the amount of scattering is imperative for increased confidence in detecting such signals and overall enhanced detector sensitivity.

The paper is composed as follows. In section 2 we give an overview of the sensors and instruments at the LIGO end stations. Next in section 3, we discuss scattering noise and mathematically define the phase and amplitude component of the noise. Scattering noise during O3

is addressed in section 4. In section 5 we provide a mathematical treatment of slow scattering, a sub-population of the light scattering and discuss the source of the noise. In section 6 we develop a method to mitigate the slow scattering noise discussed in section 5. section 7 introduces another source of slow scattering observed during O3. In section 8 we discuss a method to identify scattering times. Finally we summarize the paper in section 9.

2. Hardware and sensors at LIGO end stations

The site of light scattering discussed in this paper, is the set of mirrors located in the end station housing. This section describes these mirrors and other hardware, crucial for an understanding of light scattering. A schematic of the LIGO end station housing one end test mass (ETM) [21] of the interferometer arm is shown in figure 2. Each station has a reference seismometer on the floor to monitor ambient seismic noise. The vacuum system has at the end of the 4 km arms large vacuum chambers housing the test masses. The test mass and a transmitted light monitoring table are suspended from a two-stage seismic isolation table [22]. The test mass has a double chain, four-layered suspension for additional isolation [23]. The quadruple suspension chain behind the quadruple test mass suspension is called the reaction chain. There is additional hardware around the suspension, most importantly the ‘cage’: a structure hard bolted to the seismic isolation table which serves both as a reference and as a safety measure for protecting against large motions that could damage the suspension.

The suspension for the test mass uses OSEM at the top three stages as well as an electrostatic drive (ESD) at the test mass stage. The OSEMs at the top stages measure relative motion and can apply a force between the cage and the two chains. For the upper-intermediate mass (UIM) and penultimate (PUM) mass stages, the OSEMs measure and actuate in-between the two chains.

The transmission monitor is a double suspension with OSEMs at the top stage, measuring motion with respect to its cage [24]. It houses a telescope to reduce the large beam size coming from the arm. The LIGO end test masses have a transmission of approximately 4 ppm, so for an arm power of 250 kW as in O3a for the Livingston detector, the transmitted beam would be about 1 W. 95% of this light is dumped and 5% is split about equally between two quadrant photodiodes.

In order to keep the optical cavities in the arms on resonance, LIGO uses the interferometric signal at the detector output to sense the difference in the arm length. It then feeds back that signal to one of the end test masses, at different stages of the quadruple suspension, with a bandwidth of about 60 Hz [6]. As a result, the test mass chain moves much more relative to the local surfaces, since it has to ‘account’ for the motion of all other test masses. The main pendulum frequency of the quadruple suspension is around 0.45 Hz which means that for the force applied at frequencies below 0.45 Hz at upper stages, the entire chain will move together. The dominant ground motion to be fed back is indeed below this frequency. Furthermore, because most of the force is applied in between the chains, the test mass chain moves twice as much relative to the reaction chain. The test mass motion relative to other surfaces like the transmission monitor, the cage or the vacuum chamber walls is half of the motion measured by the OSEM at the UIM or PUM level, below 0.45 Hz.

Each LIGO detector is equipped with several hundreds of auxiliary sensors, used in the feedback control system and in the environmental monitoring system. Many of these channels are not sensitive to differential arm length and are used to identify various environmental and physical couplings to the detector. Ground motion in various frequency bands, for example, is measured by seismometers located at end stations and corner station. These seismometers record ground motion in X , Y and Z direction in the frequency range from 0.03 Hz to 30 Hz.

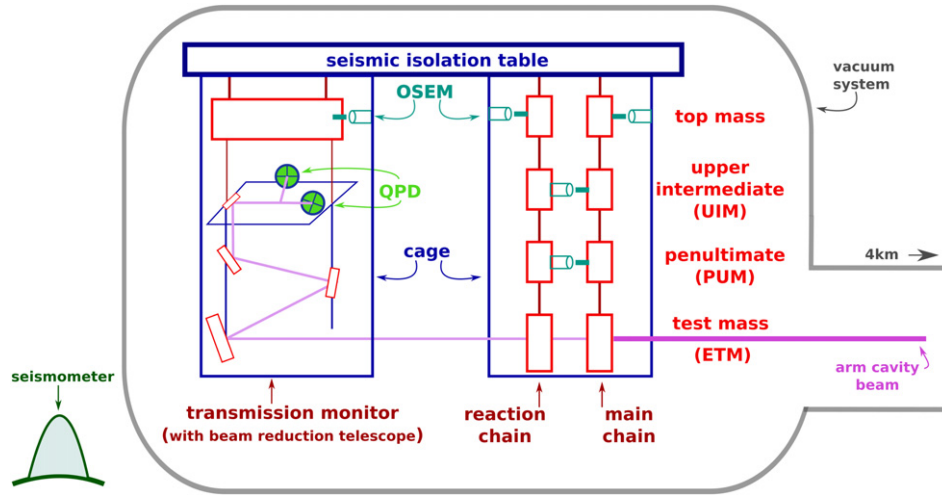


Figure 2. The schematic of end station housing shows the seismic isolation system, quadruple suspension, transmission monitor system (TMS), and the seismometer used to measure ground vibrations. The optical shadow sensor and magnetic actuators (OSEMs) in the quadruple suspension cage measure relative motion and produce a force on the main and reaction chain. About 4 ppm of the light power in the arms is transmitted through the ETM. 95% of this 4 ppm is dumped and the remaining 5% is split onto the two-quadrant photo-diodes (QPDs) in the TMS. These QPD's are used to check for any misalignment of the beam on the ETM.

Earthquakes shake the ground in 0.03–0.1 Hz band while seismic noise due to trains and human activity near the site, also known as anthropogenic noise, shows up in the 1–3 Hz region. Ocean waves and sea storms produce seismic waves with frequencies ranging from 0.03–0.5 Hz, also known as microseisms. While the secondary, and dominant, microseism peak is typically measured around 0.15 Hz [25, 26], it varies in frequencies and was strongest at 0.13 Hz for this analysis. As we discuss later, the output of these sensors is used to look for correlations with noise transients in the strain data.

3. Scattering noise

Tiny imperfections on the surfaces of test mass mirrors in the interferometer cause a small amount of light to scatter out of the main beam. This scattered light can then reflect from surfaces that have large relative motion relative to the test mass such as the chamber walls and then back to the test mass. Upon recombining with the main beam, the scattered light introduces noise in the gravitational wave data. The amplitude of the noise depends on how much light recombines with the main beam, and the upper frequency depends on the relative motion.

The motion of the scatterer introduces an additional phase in the field reflected from its surface. Consider a small fraction A of the total field that gets scattered back to the main beam, from a scattering surface located behind the ETM. This light will acquire an additional phase due to the path length modulation caused by the relative motion between the ETM and the scatterer. The resulting phase noise can be formulated as:

$$h_{\text{ph}}(f) = A \frac{\lambda}{8\pi L} \mathcal{F}[\sin \delta\phi(t)] \quad (1)$$

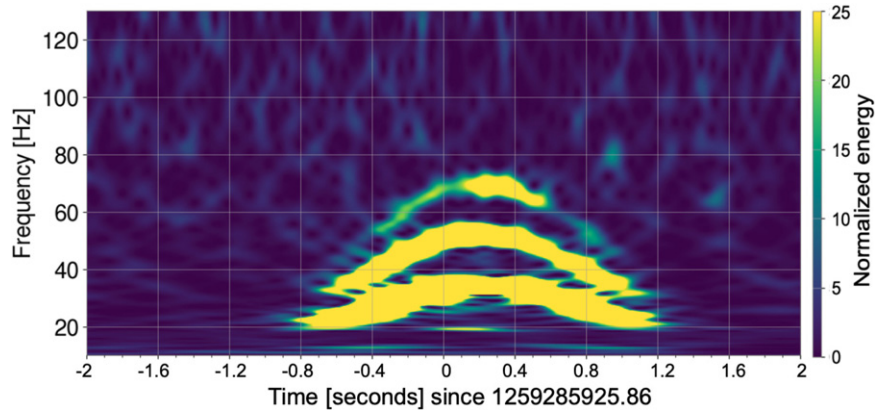


Figure 3. Scattering noise shows up as arches in the time-frequency spectrograms also known as Q-scan of the primary gravitational wave channel as processed by **gwdetchar-omega** [31, 32]. The stacked arches suggests a scatter path that involves multiple reflections of stray light between the test mass and the scatterer.

$$\phi(t) = \phi_0 + \delta\phi_{sc}(t) = \frac{4\pi}{\lambda} |x_0 + \delta x_{sc}(t)| \quad (2)$$

λ is the laser wavelength, x_0 is static path that corresponds to the static phase ϕ_0 while δx_{sc} is the time-dependent displacement of the scattering surface which gives rise to additional phase $\delta\phi_{sc}(t)$, \mathcal{F} is the Fourier transform [27–29].

The build up of this phase shifted field in the arms by the factor Γ pushes on the mirrors resulting in radiation pressure noise. This radiation component of the noise can be expressed as:

$$h_{rad}(f) = A \frac{2\Gamma P}{Mc} \frac{2}{\Omega^2 - \omega^2} \mathcal{F}[\cos \delta\phi(t)] \quad (3)$$

$\Gamma = 13.58$ here is cavity signal gain, $M = 40$ kg is the mass of mirrors, P is the power in the arms, c is speed of light and Ω is the suspension eigenfrequency [30].

Scattering noise can be recognized as arches in the Q-scan as shown in figure 3. The peak frequency of these arches tells us the number of fringes per second and can be related to the velocity of the scatterer, v_{sc} with the following relation:

$$f_{fringe}(t) = \left| \frac{2nv_{sc}(t)}{\lambda} \right| \quad (4)$$

where $f_{fringe}(t)$ is the fringe frequency and n is the number of times stray light gets reflected back and forth between the test mass and the scatterer before it joins the main beam. This equation can be derived by calculating the rate of change of phase from equation (2). We can also look at the spacing of the peaks in the time domain to give us half the period of the scattering surface.

4. Scattering in O3

The BNS range defined as the radius of the orientation-averaged spacetime volume assuming a matched-filter detection signal-to-noise ratio threshold of 8, increased to 110–140 Mpc in O3,

Table 1. Comparison of slow and fast scattering triggers in O3a at LLO as identified by GravitySpy above a confidence of 90% and SNR above 10. Frequency of arches relates to the frequency of the ground motion band active during the noise. Slow scattering is dominant during ground motion in the microseism band (0.1–0.3) Hz, whereas Fast scattering is more common during high ground motion in the anthropogenic band (1–5) Hz. This comparison is shown for LLO since at LHO, fast scattering amounts to only 1.6% of the total scattering observed. This is primarily due to difference in ground motion in anthropogenic band between the two sites.

Properties	Slow scattering triggers	Fast scattering triggers
Frequency of arches	Below 0.2 Hz	Between 2 and 5 Hz
Median SNR	37.6	11.0
Median duration	3.2 s	1.3 s
% of total scattering	40.27%	59.73%

from 80–100 Mpc in O2 [11] Due to this improvement in sensitivity and the enhanced stability of the interferometer which allows the detector to stay operational during high microseismic activity, some of the transients of similar origin in O2 and O3 now surface with higher SNR. Consequently, we see a lot more scattering arches in O3. An interesting feature of scattering in O3 is the presence of two different populations of scattering triggers, so-called the ‘slow’ scattering and the ‘fast’ scattering at both LLO and LHO. The glitch morphology of the slow scattering is the more familiar arch in Q-scan as shown in figure 3. The fast scattering triggers are more localized in time and occur with lower SNR compared to slow scattering. Table 1 compares different characteristics of slow and fast scattering triggers as classified by a noise classification tool GravitySpy discussed in section 8.

4.1. Slow scattering

In time-frequency spectrograms, slow scattering triggers resemble an arch. Figure 4(a) shows slow scattering in $h(t)$ for a day with large ground motion. As shown in this figure, the scatterer has a period of ~ 7 s, and from this we can derive the scattering surface is moving with a frequency close to 0.13 Hz which corresponds to one of the peaks in microseism [33]. Slow scattering is dominant during high ground motion in 0.03–0.1 Hz (earthquake) and 0.1–0.3 Hz (microseism) band. These arches reach high frequencies during larger ground motion and so it is more visible above the quiet background noise in the differential arm cavity (DARM). During O3, it was particularly strong on December 1, 2019 and January 6, 2020 due to high levels of ground motion on both of these days at LLO. Depending on the ground motion, slow scattering creates ‘scatter shelves’ in the frequency band 10 Hz to 120 Hz in $h(t)$ spectra.

4.2. Fast scattering

The fast scattering triggers shown in figure 5(a) occur with a frequency ~ 4 Hz [34]. This population of scattering correlates with increased ground motion in the 1–5 Hz (anthropogenic) and 0.1–0.3 Hz (microseism) band. It is normally higher in the daytime during the weekdays. Human activity near the site and trains passing on the track near the Y end station at LLO shakes the ground in these frequency bands. These triggers affect the $h(t)$ sensitivity in the band between 10 and 50 Hz.

The striking differences in the glitch morphology, SNR, and the duration for slow and fast scattering triggers suggest that they are due to different noise coupling mechanisms. Figure 6 shows the SNR and duration of total scattering triggers in O3a. Both distributions reveal the

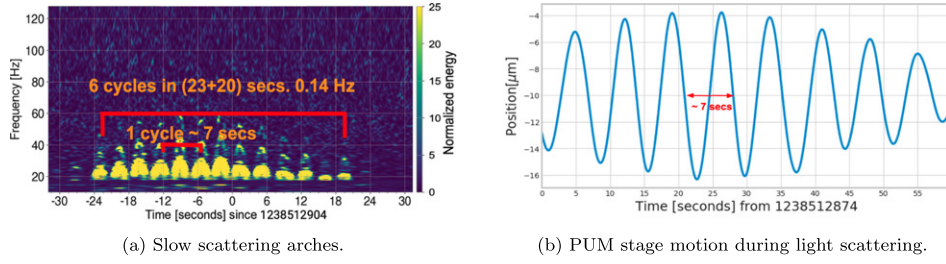


Figure 4. The left image shows Q-scan of slow scattering in the primary gravitational wave channel. This is an unusual number of arches due to extremely high ground motion in the 0.03–0.1 Hz (earthquake) and 0.1–0.3 Hz (microseism) bands on April 5, 2019. The right image shows the PUM stage motion between the chains for the same time period. As mentioned in section 2, the PUM stage OSEM records twice the displacement of the main chain.

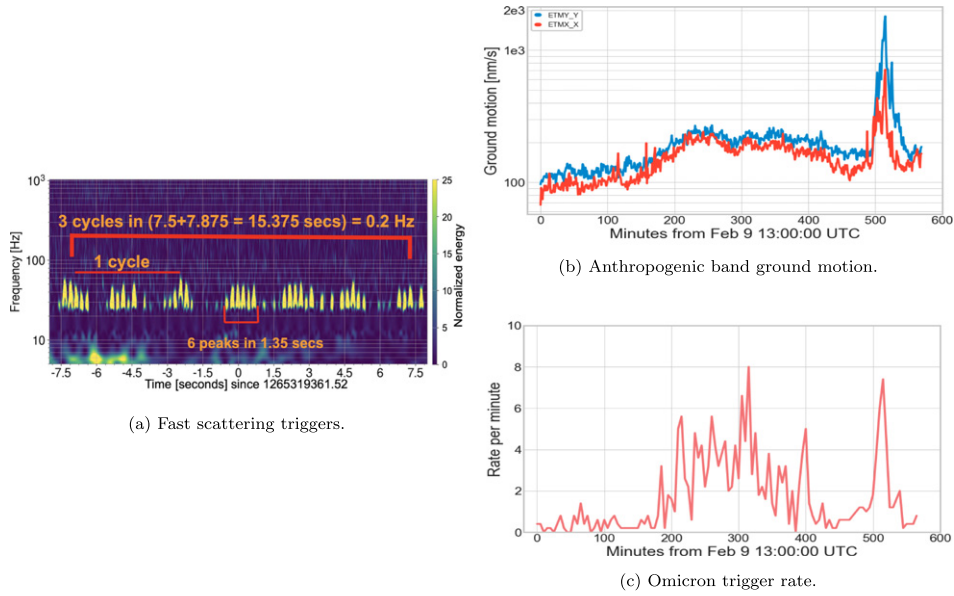


Figure 5. The left image shows Q-scan of fast scattering triggers in primary gravitational wave channel at LLO. Each ‘arch’ contains multiple sub-arches. Fast scattering triggers correlate well with high ground motion in the 1–5 Hz (anthropogenic) band. The top right image shows the ground motion in the anthropogenic band at *X* and *Y* end of the detector at LLO on February, 9, 2020. The bottom right image shows the rate of omicron triggers in the frequency band 10 to 50 Hz for the same duration.

presence of more than one population of scattering triggers. We concentrate in this paper on slow scattering triggers and will not investigate fast scattering further. In the next section, we provide a detailed description of slow scattering noise.

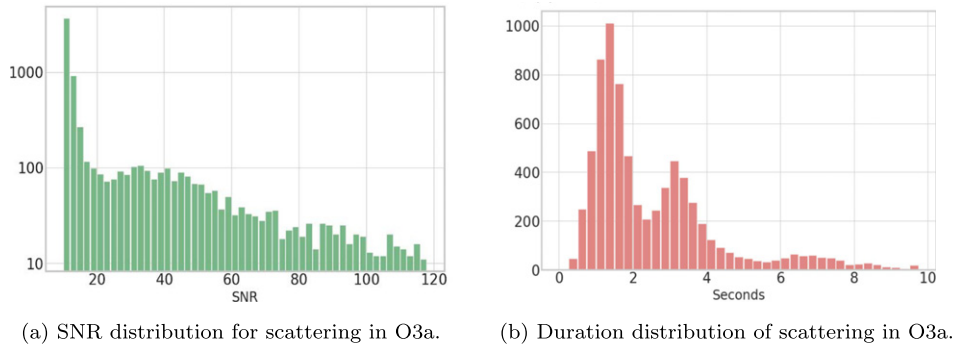


Figure 6. The SNR and duration histograms for total scattering in O3a at LLO reveal the presence of two populations the fast and slow scattering. Slow scattering tends to be louder and long duration. It should be emphasized that the third bump in the duration plot between 6 s and 8 s does not correspond to any third population, but rather to extended slow scattering. This is common when high ground motion persists long enough without the interferometer breaking lock.

5. Slow scattering noise coupling mechanism

For most of the first three aLIGO observing runs, slow scattering noise occasionally polluted the $h(t)$ spectra during periods of high ground motion in 0.1–0.3 Hz band. The characteristic scattering arches indicated that there were wavelength-scale or larger modulations of the scattering path. As described in section 2 an external drive is applied to the test mass chain to keep the optical cavities on resonance. Because the ground moves differently at the ends of the 4 km long cavities, this drive can lead to micron-scale relative motion between the ETM and other objects in its vicinity, making this region a good candidate for the source of scattering arches.

Several clues pointed specifically toward a scattering path involving the annular end reaction mass (AERM): first, the presence of several harmonics of the arches or scattering shelves, indicated that significant fractions of the light traversed the scattered light path more than once. This eliminated several potential paths, such as to light baffles or enclosure walls, because imperfect reflections on these other paths would likely cause the loss of much more than 90% of the power in each successive round trip. Second, the observation of similar harmonic series of arches at both LHO and LLO suggested that the noise was not due to an improbable alignment. And, third, micron-scale relative motions were recognized between upper stages of the test mass and reaction mass chains, suggesting that the scattering surfaces were likely between the chains. The relative movement between the ETM and AERM, δx_{sc} in equation (2), is not directly sensed, but at low frequencies (relative to the 45 Hz pendulum resonance) the motion between the ETM and AERM is similar to the motion that is sensed at the PUM stage of the compound pendulum. This allows us to approximate the motion between the ETM and the reaction mass with that of PUM stage. As shown in figure 8(a) the fringe frequency of the PUM stage motion and its higher harmonics, calculated using equation (4), match scattering arches in $h(t)$ spectrograms.

On the AERM an ESD is formed by the installation of 5 gold traces [35]. Applying a voltage on the gold traces, an electrostatic force can drive the test mass. The reaction mass is a hollow cylinder to allow the transmitted beam to pass without encountering additional optical surfaces [36]. During operations, most of the light transmitted through the ETM goes through

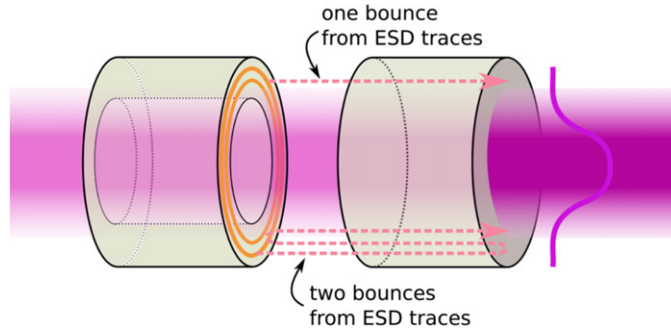


Figure 7. The reaction chain pushes on the main chain to keep the detector on resonance. Control is applied via coil actuators as shown in figure 2 and ESD as shown here. This fluctuates the distance between the AERM shown on the left and ETM shown on the right. A part of the light reflected back from the gold ESD joins the main beam in the arm with an additional phase. The changing difference in the phase between the two beams introduces noise by causing light modulation at the gravitational wave detection port. Multiple bounces between the ESD trace and the ETM show up as multiple arches in the $h(t)$ spectrograms.

the reaction mass hole and onto the other side of the reaction chain as shown in figure 7. A small fraction of this Gaussian beam hits the gold trace ESD, on the AERM. Due to its high reflectivity, almost all of the light is back scattered toward the test mass and a fraction of that is transmitted back to the arm through the ETM. This back scattered field with an additional phase shift, given by equation (2), interferes with the main beam in the arms and introduces phase noise in $h(t)$.

Let E_0 be the field in the arms and E_{esd} is the part of this field backscattered from the end reaction mass at the point E_0 is computed. We can calculate the total field in the arms:

$$E_{\text{tot}} = E_0 + E_{\text{esd}} \quad (5)$$

$$E_{\text{esd}} = E_0 A e^{i\delta\phi(t)}, \quad A = T_{\text{end}} \sqrt{f_r} \quad (6)$$

$$E_{\text{tot}} = E_0 [1 + A e^{i\delta\phi(t)}] \quad (7)$$

T_{end} is the ETM transmission (4×10^{-6}), f_r is the fraction of the power incident on the gold trace ESD. The calculation for E_{esd} involves two transmissions through the ETM and one reflection from the ESD.

The phase noise $h_{\text{ph}}(f)$ and the radiation noise $h_{\text{rad}}(f)$ due to this back scattered field is given by the equations (1) and (3) respectively. The total effective displacement power spectrum $S(f)$ can be obtained by adding the individual contributions:

$$S(f) = \sqrt{h_{\text{ph}}(f)^2 + h_{\text{rad}}(f)^2} \quad (8)$$

Figure 8(b) shows the total power spectrum for a scattering event on January 6, 2020 at LLO. The first shelf in the $h(t)$ spectrum matches for $\sqrt{f_r} = 2 \times 10^{-4}$, roughly consistent, within an order of magnitude with a previous estimation [37]. The coefficient for second and third shelf are 5×10^{-5} and 5×10^{-6} respectively, about an order of magnitude reduction for each higher harmonic. The amplitude of the scatter shelf for $(n+1)$ th harmonic is approximately 10% of n th harmonic, as suggested by these reflection coefficients. This can also be observed

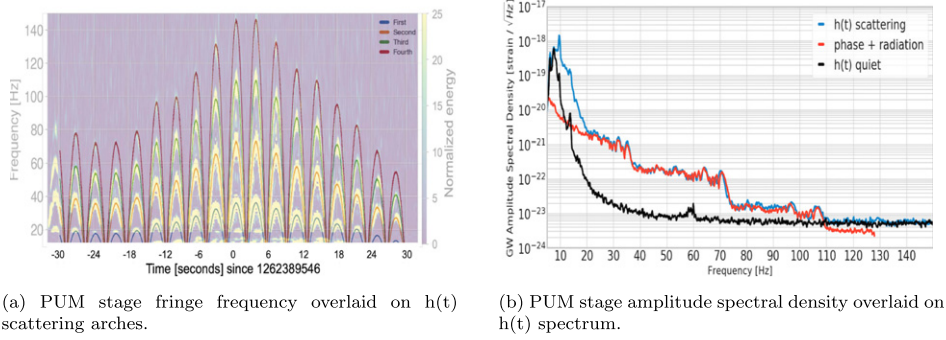


Figure 8. In the left figure, we have overlaid the multiple harmonics of the fringe frequency due to the PUM stage motion onto scattering arches. In the right figure, we have plotted the DARM spectrum during the scattering noise shown in the left figure and the spectrum calculated from the PUM stage motion using equation (8). DARM spectrum during a quieter time is shown as the black curve for comparison. The arches in the spectrogram on the left show up as shelves in the spectra on the right. Also, notice that the height for each successive shelf falls by a factor of 10. As we discuss in section 7, the scattering noise in the region below 20 Hz that does not match the red curve in the right image, is due to another slow scattering coupling.

in figure 8(b). We performed similar analysis for several scattering triggers and we found the second and third shelf coefficient magnitudes in the range of $(5 \times 10^{-5}, 6 \times 10^{-5})$ and $(5 \times 10^{-6}, 6 \times 10^{-6})$ respectively, while the first shelf coefficient did not vary.

6. Noise mitigation using suspensions control system

Scattered light due to the large relative motion between the test mass chain and reaction chain during high ground motion has adversely affected the sensitivity of the detector. One way to reduce this noise coupling is by reducing the relative motion between the ETM and AERM while keeping the intended relative motion between the ETM and the input test mass in the arm cavity. This can be achieved by sending a part of the drive from the PUM stage and feeding it to the top stage as shown in figure 2. This will cause the two chains to move together and hence will reduce the relative motion between them. The reaction chain ‘tracks’ the main chain and we call this RC tracking [38]. The reduced relative motion effectively decreases the frequency at which scattering creates shelves in $h(t)$ spectrum.

RC tracking was implemented on January 7, 2020, at LLO [39]. To understand the impact of the tracking on slow scattering caused by ETM-AERM relative motion, we measured the SNR of scattering triggers and ground motion in the earthquake and microseism band between November 1, 2019, the start of O3b and February 8, 2020. We analyze triggers that are classified as scattering by GravitySpy with a confidence above 0.9 [40]. We divided this data into pre and post RC, where for LLO pre RC is from November 1, 2019, to January 6, 2020, and post RC is from January 10, 2020, to February 8, 2020, and for LHO pre RC is from November 1, 2019, to January 14, 2020, and post RC is from January 15, 2020, to February 28, 2020. The analyzed data is normalized by the observing duration of post RC considered in this study, which is ~ 21 d for LLO and ~ 34 d for LHO. Next, we considered time segments during which the ground motion in the microseismic band is similar pre and post RC tracking and plotted the SNR distribution of scattering triggers during these time segments. We found a clear reduction

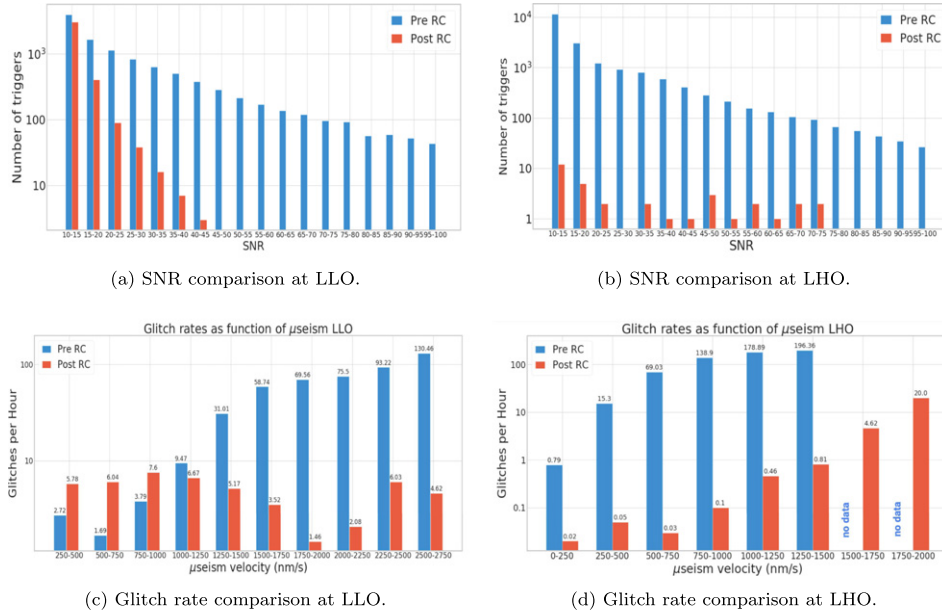


Figure 9. The top images compares the SNR of scattering triggers before and after RC tracking for LLO and LHO. The SNR distribution is plotted during similar levels of before and after ground motion in the microseism band. The bottom plots compare the scattering glitch rates for different levels of microseismic ground motion before and after RC tracking. For the pre RC tracking microseismic ground motion data considered for LHO in this study, no data was found above $1500 \mu\text{m s}^{-1}$. The scattering triggers for these plots were fetched from GravitySpy with confidence above 0.9 and SNR above 10.

in the SNR of the scattering triggers at LLO and LHO for the post RC scattering [41]. At LLO for example, the number of triggers in the SNR bin 20–25 after RC tracking is 89, while for the same bin, before RC tracking, LLO registered 1127 scattering triggers. The SNR comparison is shown in figures 9(a) and (b).

We also compared the rate of scattering triggers against the microseismic ground motion for pre and post RC tracking. Here again, we found that for similar levels of microseism above $1 \mu\text{m s}^{-1}$, the post RC glitch rates are considerably lower at both the sites as shown in figures 9(c) and (d) [42]. As can be seen from these figures, the ground motion in the microseismic band is usually higher at LLO than at LHO.

7. Relative motion between test mass and transmitted light monitors

As mentioned in section 2, the control drive sent to the ETM chain creates relative motion between the test mass and all other objects in its vicinity, such as the AERM, the TMS, vacuum chamber walls, or mechanical structures. When motion is high enough, the phase modulation from this path length difference can show up as scattering arches in both $h(t)$ and the transmitted light monitors, labeled QPD in figure 2. The motion between the main and reaction chain is twice compared to the motion between test mass and all other objects. Thus, the scattering shelf/arch due to ETM-TMS relative motion is observed at one-half the frequency of the scattering shelf/arch due to ETM-AERM relative motion. This can be seen in figure 10(a) where the first harmonic due to ETM-AERM scattering is at 40 Hz and the scattering arch

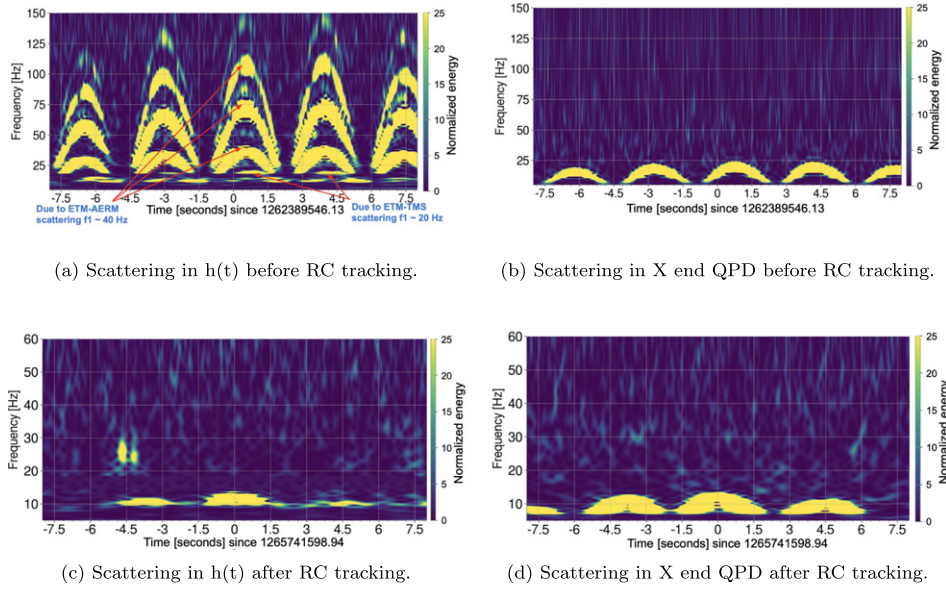


Figure 10. The top left plot shows scattering arches in $h(t)$ Q-scan during a day with very high microseism. Multiple reflections between the test mass and reaction mass generates the multiple harmonics. The first harmonic of the light scattering due to ETM-AERM relative motion is close to 40 Hz with higher harmonics present at ~ 80 Hz, ~ 120 Hz. Since the relative motion between the test mass and TMS is one-half of the ETM-AERM motion, the scattering arch due to ETM-TMS scattering is at ~ 20 Hz. The top right plot shows this scattering arch in the transmitted light monitor. After RC tracking was implemented the noise due to ETM-AERM relative motion has reduced considerably. And thus during high ground motion post RC tracking, only the ETM-TMS noise coupling shows up as scattering arches in $h(t)$ and the transmitted light monitor as shown in the bottom plots.

due to ETM-TMS scattering is at 20 Hz. Before RC tracking, a scattering shelf in transmitted light monitor at f Hz will predict scattering shelves in $h(t)$ at f Hz due to ETM-TMS coupling and at $2f$, $4f$, $6f$ and so on due to ETM-AERM coupling. Following RC tracking, a shelf in transmitted light monitor at f Hz only corresponds to a shelf in $h(t)$ at the same frequency.

Figure 10(c) shows a slow scattering arch in the time-frequency representation, after the RC tracking was implemented. The lack of multiple arches suggests that the scattering path does not involve multiple traversals between the test mass and the scatterer. The TMS-ETM scatter mechanism was confirmed experimentally. Low frequency motion was injected at the Y end seismic isolation table, forcing the DARM loop to respond by inducing large motion at the X ETM and creating a scatter shelf in $h(t)$. The TMS was then fed the same motion, reducing the relative motion in between it and the optic and the $h(t)$ scatter shelf disappeared [43–45].

With RC tracking the higher frequency scattering shelves due to ETM-AERM coupling have gone away. Figure 11 compares the scattering shelves in $h(t)$ and X end transmitted light monitor for scattering events before and after RC tracking. The DARM control signal is sent to one test mass and this results in large relative motion between the test mass and its surroundings. One remedy to reduce the ETM-TMS relative motion is to split and apply this

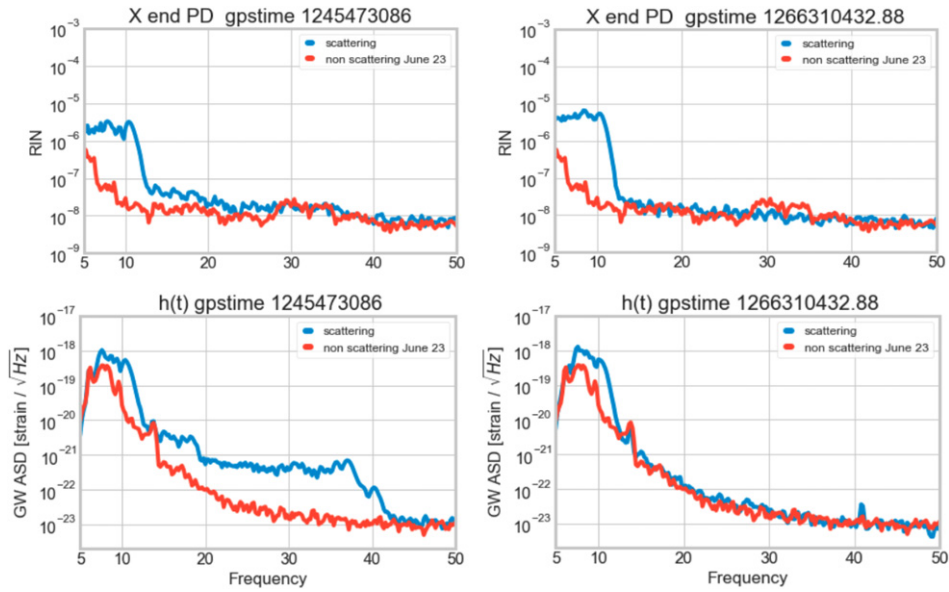


Figure 11. The left image shows relative intensity noise of X end transmitted light monitor and $h(t)$ before RC tracking was implemented. The scattering shelf at 10 Hz in $h(t)$ correlates with ETM-TMS noise coupling, while the higher frequency shelves at ~ 20 Hz and ~ 40 Hz are due to ETM-AERM scattering. The image on the right is for a post RC tracking scattering event and higher frequency shelves are absent in $h(t)$ due to reduced relative motion between the main chain and the reaction chain.

control drive at all four test masses forming the LIGO arm cavities. This will reduce the relative motion by a factor of 4. Further reduction can be employed by making the TMS follow the test mass chain like in the test described above and we intend to implement this for the next observing run.

8. Using transmitted light monitors to identify scattering

GravitySpy is an image recognition tool that uses machine learning to classify the variety of omicron triggers that show up as transient noise in the strain data. It is a citizen science project and volunteers help to generate the training dataset by assigning one of the several glitch classes to the spectrogram images. The algorithm assigns each image a glitch class and a confidence score which represents the probability that the image belongs to that specific glitch class. We can identify times of transients due to scattered light by looking at the output of GravitySpy [40, 46].

8.1. GWDetChar-scattering

Another way of identifying the potential scattering triggers is by monitoring the motion of OSEMs and then correlating it with the presence of the same triggers in the gravitational wave strain channel. This is accomplished by using an algorithm called—**gwdetchar-scattering** [32]. Throughout the detector, OSEMs are used to capture the motion of any components, light can get scattered from. The timeseries data from these sensors is used to find potential site of scattering in the following way. The position measurements taken by the OSEMs is first

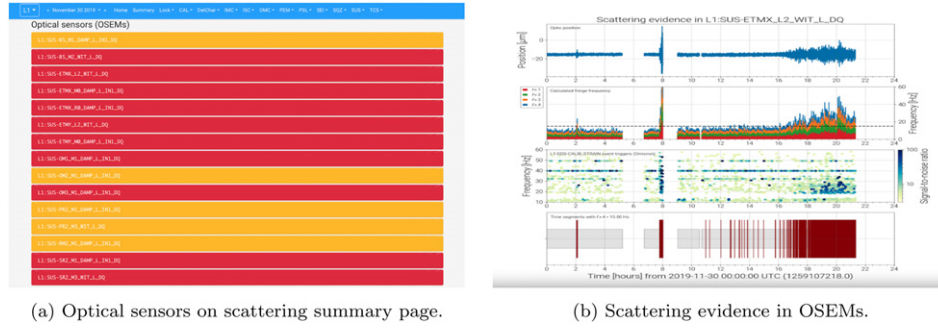


Figure 12. The left image shows the optical sensors processed by **gwdetchar-scattering** for evidence of scattering. They are colour coded with red for strong evidence of scattering and yellow for weak. The topmost plot on the right image shows the position measurement by the OSEM on the PUM stage of the reaction chain, followed by the fringe frequency calculated using 4. The third plot shows $h(t)$ Omicron glitches with the glitch rate increasing with the increase in fringe frequency motion. The final plot shows the time segments during which the fringe frequency motion is above 15 Hz. The $h(t)$ triggers that lie within these scattering segments are written to a file as potential scattering.

converted velocity using a savgol filter [47] and then to fringe frequency using the following equation (4). The **gwdetchar-scattering** script then creates segments of the form (starttime, endtime) during which the fringe frequency motion in optic crosses a certain frequency threshold. The algorithm then looks for time coincidences between these segments and omicron triggers in $h(t)$ in 10–60 Hz frequency band. Efficiency is defined as the percentage of triggers in $h(t)$ channel that falls within these segments while the deadtime is the duration of all the segments for an optic as a percentage of total observing time. An optic is considered to be ‘strong’ witness if the ratio of efficiency over deadtime is greater than 2 and ‘weak’ if it is less than 2. The script then prepares a webpage, as shown in figure 12, showing the movement of all the optics, the scattering segments of each optic and the information of $h(t)$ triggers captured by these segments [48].

Another method to identify scattering culprits is to employ an adaptive algorithm based on time varying empirical mode decomposition (tvf EMD) used at Virgo [49]. This method which utilizes the non-linear nature of light scattering, finds correlation between the instantaneous amplitude of primary channel and time derivative of potential scatterer’s position. A method based on Hilbert Huang transform has also been developed to catch scattering surfaces [50]. The tvf EMD and the Hilbert Huang methods are based on quantifying time series correlation between the gravitational strain data and potential scattering surface. The **gwdetchar-scattering** finds time coincidence between moving optical surfaces and trigger data processed by another pipeline (Omicron).

GravitySpy, even though does not provide any information with regards to where the scatterer might be located, identifies a larger subset of scattering triggers compared to that identified by motion in OSEMs. On the other hand, optics motion can be a more direct method of locating the source of scattering noise since it can identify which mirror is moving with the velocity required. It thus makes sense to see if we can make **gwdetchar-scattering** more ‘efficient’ by adding better scattering witnesses to the algorithm. In this section, we explore such a witness that can be used to identify the scattering noise.

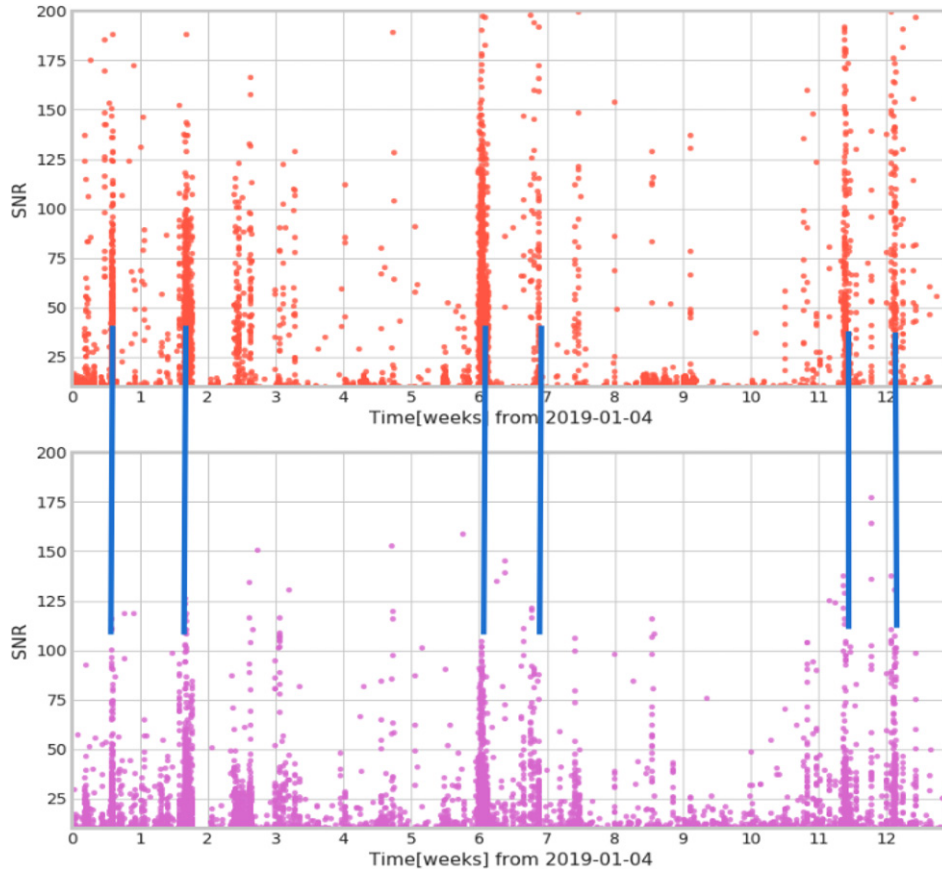


Figure 13. Time coincidence between X end transmitted light monitor and slow scattering in $h(t)$ channel during the first three months of O3a at LLO. The top plot shows slow scattering triggers identified by GravitySpy above a confidence of 0.95 in $h(t)$ and the bottom plot shows the omicron triggers in X end transmitted light monitor during the same time period. The vertical lines show the correlation between the scattering in $h(t)$ channel and noise in the transmitted light monitor channel.

In section 7, we showed that the transmitted light monitors serve as a witness of slow scattering noise in $h(t)$. Figure 13 shows a time correlation between the slow scattering triggers in $h(t)$ as identified by GravitySpy and the noise in the transmitted light monitor below 20 Hz. Due to the presence of this temporal coincidence of triggers, the noise in this auxiliary channel can be used to identify the slow scattering noise in $h(t)$. These channels can be added to the list of optics, over which the algorithm **gwdetchar-scattering** iterates to find scattering in $h(t)$. This change represents an update on **gwdetchar-scattering** rather than a new algorithm to find scattering noise.

Apart from slow scattering, ‘extremely loud triggers’, which is another class of triggers characterized by typically high SNR, also makes its way to the transmitted light monitors. The source of these loud triggers is not well understood but it is not believed to be related to scattered light, so we need to remove these triggers from our analysis. To differentiate the presence of slow scattering noise in $h(t)$ from loud triggers, we can look at the frequency content of the coincident noise in the transmitted light monitors. The scattering noise in these witness

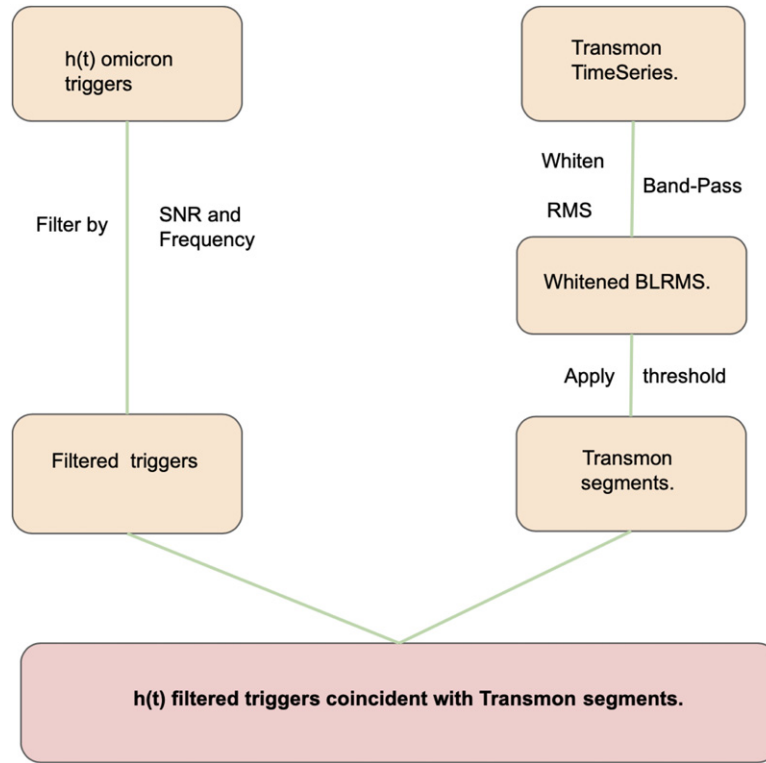


Figure 14. Flowchart of the process to capture scattering in $h(t)$ by using segments generated from whitened transmon BLRMS. Transmon or transmitted light monitor's time series is first whitened to normalize the power in the frequency bins. This is followed by band-passing the data between 4 and 10 Hz. Since the scattering arches show up in this frequency range in the transmon, band-passing will remove any noise outside this range. After taking the root-mean-square, any values of this whitened and band-passed time-series above a given threshold are converted to segments. We then look for coincidence between these BLRMS segments and $h(t)$ omicron triggers filtered by SNR and frequency.

channels appears in the range 4–10 Hz while the triggers coincident with loud glitches in $h(t)$ typically appear with higher peak frequency.

8.2. Band-limited RMS

To capture the scattering triggers in $h(t)$, we use whitened band-limited root mean square (RMS) segments constructed from the raw time-series of the transmitted light monitors, in the frequency band of interest. A scattering trigger in $h(t)$ shows up as a spike in these band-limited RMS (BLRMS). By choosing a suitable threshold, we can create BLRMS segments and then use time coincidence with the Omicron triggers in $h(t)$ to identify the scattering triggers. Any $h(t)$ triggers that coincide with these band-limited segments are then written to a file as potential scattering. This process is shown in figure 14. Before finding time coincidence between the $h(t)$ triggers and BLRMS segments, we filter the triggers by SNR (between 15 and 200) and frequency (between 10 Hz and 60 Hz), thus excluding the loud triggers that can pollute the algorithm. The transmitted light monitors witness loud slow scattering as 95% of

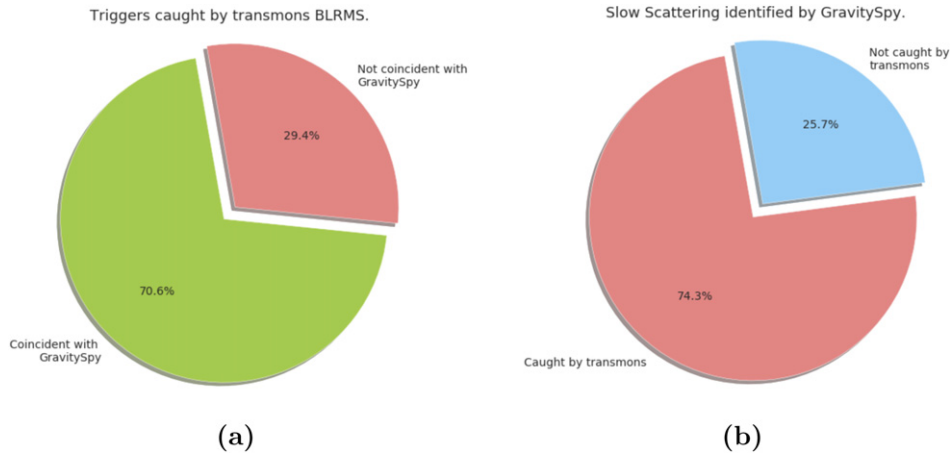


Figure 15. For O3a, the first pie chart shows that most of the triggers vetoed by BLRMS segments are identified as scattering by GravitySpy above a confidence of 0.8. The spectrograms of a subset of false positives show most of them are slow scattering but were labelled with a confidence lower than 0.8 by GravitySpy. The second pie chart shows that BLRMS segments caught close to 75% of the slow scattering that GravitySpy identified above a confidence of 0.8.

the light transmitted through the ETM is dumped before it reaches the TMS, hence we use a lower SNR limit of 15 .

We performed the analysis for O3a, from April 1, 2019, to September 30, 2019. The BLRMS segments identified 3864 $h(t)$ triggers as scattering at LLO while GravitySpy found 3663 scattering triggers above confidence of 0.8. As shown in figure 15b three-fourth of the GravitySpy scattering match with scattering triggers caught by BLRMS segments. 71% of the 3864 triggers caught by BLRMS segments match with GravitySpy output. This suggests that 29% of 3864 or approximately 1120 triggers are false positive with respect to GravitySpy. The time-frequency spectrograms of 57 randomly chosen trigger times from these 1120 triggers showed that as many as 40 of these were scattering triggers, but they were not labeled as scattering by GravitySpy above confidence of 0.8.

We also examined the performance of BLRMS segments against OSEM time series on 3 d in O3a dominated by slow scattering noise. Figure 16 shows the efficiency over dead time for April 13, 2019, May 13, 2019, and June 25, 2019. Efficiency is the fraction of filtered $h(t)$ triggers that coincide with BLRMS segments. Deadtime refers to the total duration of the segments as a fraction of the total observing duration for that day. A large value of efficiency over deadtime is preferred as the goal is accurate identification of noise. For all the three days, BLRMS segments register higher efficiency over deadtime than OSEMs scattering segments. The **gwdetchar-scattering** algorithm with just OSEMs as scattering witnesses, is designed to capture the motion of optics throughout the interferometer. As we have identified the likely location of scattering, we can use a more specific approach by employing the transmitted photodiode's BLRMS segments to capture the noise.

Of the two separate noise couplings mentioned in sections 5 and 7, the PUM stage OSEM is sensitive to only first of these, the ETM-AERM relative motion. And in principle we expect it to identify as much noise as the BLRMS segments. Following RC tracking however, the scattering impact due to ETM AERM relative motion has been reduced while having no effect

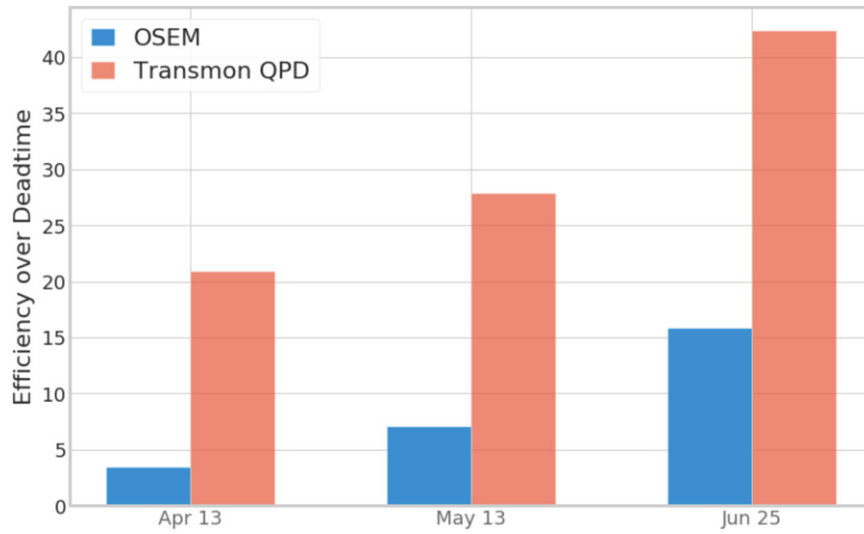


Figure 16. Comparing efficiency over deadtime between OSEMs and BLRMS segments. This shows that for slow scattering that occurred on April 13, May 13 and June 25, 2019, transmitted light monitor's band limited RMS segments perform better than OSEMs in identifying it.

on ETM TMS noise which the PUM stage is not sensitive to. Post RC tracking slow scattering noise can thus still be identified using the BLRMS segments.

9. Summary and discussion

Scattering noise affects the data quality of the advanced LIGO detectors. Upconversion of the low-frequency noise due to large optic motion reduces the sensitivity of the detector in 10–120 Hz band. We use witnesses that identify times in the data when scattering noise is present as well as, when possible, identifying and eliminating the scatter mechanism in the instrument detector itself.




We analyzed light scattering in LLO during O3 and we found the presence of two different populations of scattering noise, slow scattering, and fast scattering. We investigated slow scattering that appears with a typical arch shape in the time-frequency representation and we found two different paths through which this noise couples to the detector simultaneously. We were able to implement a solution for the louder noise coupling that resulted in a substantial reduction of the noise and we discussed possible remedies for the second one. One of these solutions, the TMS feed forward, we plan to implement in O4. In order to identify the times when this noise is present in the gravitational wave channel, we suggested using the band-limited time-series data of an auxiliary channel. This channel, monitors the light transmitted through the ETM and we showed it identifies a larger subset of scattering triggers as compared to other scattering witnesses.

High Q resonances found at the corner and end stations at LLO could be contributing to fast scattering. The ongoing investigation suggests that damping the motion of some optical components at these stations would likely mitigate the rate of fast scattering.

Acknowledgments

LIGO was constructed by the California Institute of Technology and Massachusetts Institute of Technology with funding from the National Science Foundation and operates under Cooperative Agreement No. PHY-1764464. Advanced LIGO was built under Grant No. PHY-0823459. We acknowledge support from the NSF grant PHY-1806656, PHY-1505779, and PHY-1912604. We also acknowledge the discussions with the members of Detector Characterization Group of the LIGO Scientific Collaboration. For this paper, we use the data from the advanced LIGO detectors and we used the LIGO computing clusters to perform the analysis and calculations.

ORCID iDs

S Soni  <https://orcid.org/0000-0003-3856-8534>
 C Austin  <https://orcid.org/0000-0001-5488-9480>
 G González  <https://orcid.org/0000-0003-0199-3158>

References

- [1] Aasi J *et al* (Advanced LIGO) 2015 *Class. Quantum Grav.* **32** 074001
- [2] Acernese F *et al* 2014 Advanced Virgo: a second-generation interferometric gravitational wave detector *Class. Quantum Grav.* **32** 024001
- [3] Dooley K L *et al* 2016 GEO 600 and the GEO-HF upgrade program: successes and challenges *Class. Quantum Grav.* **33** 075009
- [4] Abbott B P *et al* 2017 Calibration of the advanced LIGO detectors for the discovery of the binary black-hole merger GW150914 *Phys. Rev. D* **95** 062003
- [5] Viet A D *et al* 2018 Reconstructing the calibrated strain signal in the advanced LIGO detectors *Class. Quantum Grav.* **35** 095015
- [6] Martynov D V *et al* 2016 The sensitivity of the advanced LIGO detectors at the beginning of gravitational wave astronomy *Phys. Rev. D* **93** 112004
- [7] Abbott B P *et al* 2019 GWTC-1: a gravitational-wave transient catalog of compact binary mergers observed by LIGO and virgo during the first and second observing runs *Phys. Rev. X* **9** 031040
- [8] Abbott B P *et al* 2016 Gw150914: the advanced LIGO detectors in the era of first discoveries *Phys. Rev. Lett.* **116** 131103
- [9] Abbott B P *et al* 2017 GW170817: observation of gravitational waves from a binary neutron star inspiral *Phys. Rev. Lett.* **119** 161101
- [10] Grace D B 2019 <https://gracedb.ligo.org>
- [11] Abbott B P *et al* 2019 Prospects for observing and localizing gravitational-wave transients with advanced LIGO, advanced virgo and KAGRA (arXiv:1304.0670v9)
- [12] Massinger T J 2016 Detector characterization for advanced LIGO *PhD Thesis* Syracuse UniversityDCC document <https://dcc.ligo.org/LIGO-P1600205P1600205>
- [13] Abbott B P *et al* 2016 Characterization of transient noise in advanced LIGO relevant to gravitational wave signal GW150914 *Class. Quantum Grav.* **33** 134001
- [14] Nuttall L K 2018 Characterizing transient noise in the LIGO detectors *Phil. Trans. R. Soc. A.* **376** 20170286
- [15] Abbott B P *et al* 2020 A guide to LIGO Virgo detector noise and extraction of transient gravitational-wave signals *Class. Quantum Grav.* **37** 055002
- [16] Cabero M *et al* 2019 Blip glitches in advanced LIGO data *Class. Quantum Grav.* **36** 155010
- [17] Robinet F (Virgo Collaboration) 2018 Omicron: an algorithm to detect and characterize transient events in gravitational-wave detectors *VIR-0545C-14*

- [18] Robinet F, Arnaud N, Leroy N, Lundgren A, Duncan M and McIver J 2020 Omicron: a tool to characterize transient noise in gravitational-wave detectors *SoftwareX* accepted (<https://doi.org/10.1016/j.softx.2020.100620>)
- [19] McIver J L 2015 The impact of terrestrial noise on the detectability and reconstruction of gravitational wave signals from core-collapse supernovae *PhD Thesis* Massachusetts U., Amherst
- [20] Abbott R *et al* 2020 GW190521: a binary black hole merger with a total mass of $150 M_{\odot}$ *Phys. Rev. Lett.* **125** 101102
- [21] Pinard L *et al* 2017 Mirrors used in the LIGO interferometers for first detection of gravitational waves *Appl. Opt.* **56** C11–5
- [22] Matichard F *et al* 2015 Seismic isolation of advanced LIGO: review of strategy, instrumentation and performance *Class. Quantum Grav.* **32** 185003
- [23] Aston S M *et al* 2012 Update on quadruple suspension design for advanced LIGO *Class. Quantum Grav.* **29** 235004
- [24] Barsotti L, Evans M and Fritschel P 2010 Alignment sensing and control in advanced LIGO *Class. Quantum Grav.* **27** 084026
- [25] Cessaro R K 1994 *Sources of Primary and Secondary Microseisms*
- [26] Effler A, Schofield R M S, Frolov V V, González G, Kawabe K, Smith J R, Birch J and McCarthy R 2015 Environmental influences on the LIGO gravitational wave detectors during the 6th science run *Class. Quantum Grav.* **32** 035017
- [27] Accadia T *et al* 2010 Noise from scattered light in Virgo's second science run data *Class. Quant. Grav.* **27** 194011
- [28] Canuel B, Genin E, Vajente G and Marque J 2013 Displacement noise from back scattering and specular reflection of input optics in advanced gravitational wave detectors *Opt. Express* **21** 10546–62
- [29] Vajente G and Marque J 2014 Stray light issues in advanced interferometers and the search for gravitational waves *Astrophys. Space Sci. Libr.* **404** 275–90
- [30] Ottaway D J, Fritschel P and Waldman S J 2012 Impact of upconverted scattered light on advanced interferometric gravitational wave detectors *Opt. Express* **20** 8329–36
- [31] Chatterji S, Blackburn L, Martin G and Katsavounidis E 2004 Multiresolution techniques for the detection of gravitational-wave bursts *Class. Quantum Grav.* **21** S1809–18
- [32] Urban A L *et al* 2019 *gwdetchar/gwdetchar: 1.0.2*
- [33] Soni S *et al* 2019 Slow scattering on april 5 at L1 *alog 45053* Louisiana State University
- [34] Smith A L J 2019 Anthropogenic noise causing daily range degradation via scattering *alog 44860* California State University
- [35] Hennig M 2016 End reaction mass ESD coating face pattern *DCC Document D0900949-V2* University of Glasgow
- [36] Sanchez G B E 2015 Annular end reaction mass (AERM) *DCC document D1500163-v4* California Institute of Technology
- [37] Yamamoto H 2015 Effects of scattered light by AERM *DCC document T1500455-v2* California Institute of Technology
- [38] Schofield R *et al* 2019 Scattering noise up to 100 Hz from 0.1 Hz relative motion of test and reaction masses at LHO and LLO, and potential mitigation *alog 54298* University of Oregon
- [39] Effler A *et al* 2019 Reaction chain now tracks main chain for both ETMs *alog 50851* California Institute of Technology
- [40] Zevin M *et al* 2017 Gravity spy: integrating advanced LIGO detector characterization, machine learning, and citizen science *Class. Quantum Grav.* **34** 064003
- [41] Soni S *et al* 2019 Studying the r zero tracking effect on scattering noise *alog 51594* Louisiana State University
- [42] Austin C *et al* 2019 Rate of scattering glitches as a function of microseism *alog 51613* Louisiana State University
- [43] Effler A *et al* 2020 Microseism fringing and tmsx ff/tracking *alog 52118* California Institute of Technology
- [44] Soni S *et al* 2020 Transmon QPD's during ISI shaking test *alog 52204* Louisiana State University
- [45] van Heijningen J V 2018 Turn up the Bass! low-frequency performance improvement of seismic attenuation systems and vibration sensors for next generation gravitational wave detectors *PhD Thesis* Vrije U., Amsterdam
- [46] Bahaadini S, Noroozi V, Rohani N, Coughlin S, Zevin M, Smith J R, Kalogera V and Katsaggelos A 2018 Machine learning for gravity spy: glitch classification and dataset *Inf. Sci.* **444** 172–86

- [47] Virtanen P *et al* (SciPy 1.0 Contributors) 2020 Scipy 1.0: fundamental algorithms for scientific computing in python *Nat. Methods*
- [48] Urban A L, Duncan M, Anderson S and Baryoga J 2013 LIGO DetChar summary pages <https://summary.ligo.org>
- [49] Longo A, Bianchi S, Plastino W, Arnaud N, Chiummo A, Fiori I, Swinkels B and Was M 2020 Scattered light noise characterisation at the virgo interferometer with tvf-emd adaptive algorithm *Class. Quantum Grav.* **37** 145011
- [50] Valdes G, O'Reilly B and Diaz M 2017 A Hilbert–Huang transform method for scattering identification in LIGO *Class. Quantum Grav.* **34** 235009